Luminescence switch of Mn-Doped ZnAl2O4 powder with temperature

Lucile Cornu, Mathieu Duttine, Manuel Gaudon, Veronique Jubera

Luminescence switch of Mn-Doped $ZnAl_2O_4$ powder with temperature

L. Cornu,[ab] M. Duttine,[abcd] M. Gaudon*[ab] and V. Jubera*[ab]

Manganese-doped $ZnAl_2O_4$ phosphors were prepared by the Pechini synthesis route and treated at various temperatures from 600 to 1350 °C. The samples were characterized by TEM-EDX, XRD, EPR, and their diffuse reflectance and luminescence properties were investigated. The structural analysis showed the high solubility limit of manganese in this spinel matrix and allowed the determination of the global inversion rate, which characterizes the cation distribution in the A and B sites of the spinel structure. As the annealing temperature increased, this factor decreased leading to a more direct matrix. EPR analysis showed that, besides Mn^{3+} to Mn^{2+} reduction, the local environment of Mn^{2+} cations changed with the annealing temperature, which was also reflected in the evolution of the optical properties. As the annealing temperature increased, the red luminescence related to the presence of divalent manganese in octahedral sites faded and was replaced by a new green emission due to Mn(II) ions located in tetrahedral sites within the spinel structure. For 0.5% Mn-doped $ZnAl_2O_4$, this red to green luminescence switch occurred for samples treated between 1200 and 1350 °C. Moreover, the Al-overstoichiometric samples ($Mn:ZnAl_{2.2}O_{4+\delta}$) showed that it is possible to modify the temperature range and the kinetics of this variation in emission wavelength. These tuneable properties suggest that Mn-doped spinels are potential candidates for developing stable and highly sensitive thermal sensors.

DOI: 10.1039/XXXXXXXXXX

1. Introduction

Over the past decades, many applications for $ZnAl_2O_4$ spinel compounds have been reported, such as catalysis of hydrocarbon reactions,[1,2] sintering of alumina ceramics,[3] or improving ceramic dielectric properties.[4,5] With an energy gap of 3.8 eV, this material is also an ultraviolet absorbent and is already used in optoelectronic devices.[6] $ZnAl_2O_4$ spinel doped with transition metal ions, such as cobalt,[7–9] manganese[10–12] or rare earth elements, *e.g.* europium[13] or terbium,[14] can be used as luminescent material in flat panel displays[15] or as pigments in glazes or stoneware.[16] Indeed, its structure offers many possibilities for luminescence coloration (wavelength range of emission bands) by modulating the doping level and the location of the doping agent in the structure. Spinel compounds with the general formula AB_2O_4 crystallize in the cubic system with space group $Fd\bar{3}m$. The unit cell contains 32 oxygen ions which form 64 tetrahedral sites and 32 octahedral sites. Each unit cell is composed of eight AB_2O_4 patterns. In the direct spinel structure, only eight of the tetrahedral sites, Wyckoff positions 8a (1/8, 1/8, 1/8), and 16 of the octahedral sites, Wyckoff positions 16d (1/2, 1/2, 1/2), are occupied by the A and B cations, respectively, and the oxygen anions fully occupy the 32e positions.[11] In $ZnAl_2O_4$, also called gahnite, a non-negligible quantity of Zn^{2+} cations is located in the 16d sites and as a consequence, Al^{3+} cations may partially occupy the 8a sites. The proportion of Zn^{2+} cations in the octahedral sites is called the inversion rate (δ) and can take any value between 0 and 1. The general formula of this type of spinel phase can be written $(Zn_{1-\delta}Al_{\delta})[Al_{2-\delta}Zn_{\delta}]O_4$, in which parentheses denote the tetrahedral sites and the brackets the octahedral sites. An inversion rate varying between $0 < \delta < 0.05$ (ref. 17–19) has been reported for the $ZnAl_2O_4$ matrix. Indeed, the value of δ has clearly been shown to be dependent on the chosen synthesis route. Routes included the solid-state reaction,[20–22] tartaric complex formation as the oxide precursor,[23] a microwave-assisted hydrothermal process,[24] autocombustion using glycine/urea fuels,[14,25] sol–gel,[11] or the Pechini route.[8,26] Special care must be taken with the type of synthesis precursors and the accessible crystallite sizes as they can both affect the inversion rate of the as-prepared samples. We have recently demonstrated its evolution through the Pechini and co-precipitation synthetic routes.[27] Controlling the inversion factor of doped $ZnAl_2O_4$ materials may be of great interest, especially when the doping cation has luminescent properties that are sensitive to the crystal field strength and the coordination polyhedron, such as Mn^{2+}. Mn-doped materials have been intensively studied since the beginning of the twentieth

[a]*CNRS, ICMCB, UPR 9048, F-33600 Pessac, France. E-mail: gaudon@icmcb-bordeaux.cnrs.fr; jubera@icmcb-bordeaux.cnrs.fr*

[b]*Univ. Bordeaux, ICMCB, UPR 9048, F-33600 Pessac, France*

[c]*Sorbonne Universités, UPMC Univ Paris 06, UMR 8234, PHENIX, F-75005, Paris, France*

[d]*CNRS, UMR 8234, PHENIX, F-75005, Paris, France*

century, mainly because this transition metal ion produces an emission in the visible region and can be excited in many different ways. The luminescent emission consists of a broad band corresponding to the radiative de-excitation from the $^4T_1$ excited level to the $^6A_1$ ground state energy level. Mn^{2+} in a tetrahedral environment produces a green centered emission, whereas the luminescence is red-shifted when it is located in an octahedron. A long luminescence decay time of 100 μs to 1 ms is expected because of the change in the spin multiplicity.

In this work, Mn-doped $ZnAl_2O_4$ phases were prepared by a soft chemistry route (Pechini process) and treated at various temperatures in order to determine the relationship between the cationic distribution and crystallite sizes. On one hand, the global divalent cation inversion rate ($\delta_{Zn} + \delta_{Mn}'$, where δ_{Zn} and δ_{Mn}' are the inversion rates of zinc and manganese cations, respectively) was obtained from Rietveld refinements performed on the samples XRD-patterns after various thermal treatments. On the other hand, to detect any changes in the specific Mn(II) environment, electron paramagnetic resonance (EPR) analyses were performed. The combination of all these structural analyses and their correlation with the luminescence properties has led to an accurate understanding of the influence of thermal treatment on the cationic distribution in Mn-doped $ZnAl_2O_4$ samples.

2. Materials and methods

2.1. Preparation of compounds

The $Zn_{(1-x)}Mn_xAl_2O_4$ samples were synthesized by the Pechini route. Stoichiometric amounts of zinc nitrate hexahydrate (Alfa Aesar, Puratronic 99.998% (metal basis)), aluminum nitrate nonahydrate (Alfa Aesar, low mercury, Puratronic 99.999% (metal basis)) and manganese nitrate hydrate (Alfa Aesar, Puratronic 99.999% (metal basis)) were dissolved in mineral water. The zinc concentration of the as-prepared solution was equal to 0.8 mol L^{-1}. Citric acid (CA) and ethylene glycol (EG), used as polyesterification precursors, were added to the solution (salt : CA : EG molar ratio 1 : 4 : 4) and water was slowly evaporated by heating on a hot plate. The highly viscous mixture formed after polyesterification was annealed at 400 °C for 5 h under air to obtain a dark brown powder. Thereafter, various thermal treatments were performed between 500 and 1350 °C under air for 10 h. After this first thermal treatment, the samples were a light-yellow color. This coloration may reflect the inter-valence absorption due to the presence of manganese in oxidation states higher than (II). An additional reductive thermal treatment under a argon/dihydrogen 90–10 mol% atmosphere was then performed to reduce residual Mn(III) and Mn(IV) cations. The annealing temperature did not exceed 500 °C to avoid the occurrence of black spots on the powder surface and inside the grains. This localized dark coloring is probably due to the reduction of zinc or the formation of colored centers associated with oxygen vacancies. Moreover, from a structural point of view, the highest concentration of manganese that can substitute zinc in the matrix was investigated.

2.2. X-ray diffraction

Powder X-ray diffraction patterns were collected on a Philips X'Pert MPD X-ray diffractometer with Bragg–Brentano geometry using Cu $K\alpha_{1,2}$ radiation ($10 < 2\theta < 130°$, step: 0.02°, counting time: 30 s). The diffractograms were analyzed with the FullProf program and structural model Rietveld refinements were performed with conventional reliability factors. Unit cell parameters, atomic positions, occupancies and Debye–Waller factors were refined based on the $Fd\bar{3}m$ space group corresponding to the spinel structure and considered the various composition models referred in the text. Furthermore, because FullProf peak profile function N°7 was used, the crystallite size was directly obtained.

2.3. Transmission electron microscopy and energy-dispersive X-ray

Transmission electron microscopy (TEM) was performed on TECNAI F20 equipment with a field emissive gun, operating at 200 kV and with a point resolution of 0.24 nm. TEM samples were prepared by dissolving a few milligrams of powder in ethanol. The solution was then ultrasonicated for 10 min in order to disagglomerate and disperse the powder particles. One drop of the solution was deposited on a Formvar/Carbon copper grid. Chemical cartographies were obtained using an EDX detector.

2.4. Photoluminescence

The photoluminescence properties were analyzed using a SPEX FL212 spectrofluorimeter equipped with a 450 W xenon lamp. The excitation spectra were corrected for the variation of the incident flux as well as the emission spectra for the transmission of the monochromator and the response of the photomultiplier. This equipment was also used to record diffuse reflectance spectra. In this case, the emission and the excitation monochromator were set in a synchronous mode to collect all the diffuse reflection of the xenon lamp with no fluorescence photons. A black reference (B: black toner) and a white reference (W: magnesia, MgO) were scanned under the same conditions and the measurement from the sample (S) was corrected to obtain the desired data (D) by using the relation $D = (S - B)/(W - B)$.

2.5. Electron paramagnetic resonance

EPR spectra were recorded at room temperature with a Bruker EMX spectrometer operating at X-band frequency (9.45 GHz). The main spectroscopic parameters: microwave power, 10 mW; magnetic field modulation frequency, 100 kHz; amplitude, 0.1 mT; and spectral resolution, 0.06 mT pt^{-1}. WINEPR and SIMFONIA software were used to simulate the EPR spectra and estimate the g values and hyperfine interaction parameters. DPPH was used as external reference to calibrate the spectrometer and $CuSO_4 \cdot 5H_2O$ (Sigma-Aldrich, 99.999% (metal basis)) was used as standard sample to estimate the number of spins participating in the observed resonances.

3. Results and discussion

3.1. Mn-solubility limit in $Zn_{1-x}Mn_xAl_2O_4$ phases

The XRD patterns of the two highly doped samples ($x = 0.15$ and 0.30) show the characteristic diffraction peaks of the spinel structure (no. 00-005-0669) (Fig. 1a and b). In addition, a secondary phase attributed to the α-Al_2O_3 phase (no. 00-046-1212) was detected for the sample with the highest doping rate.

TEM-EDX analyses were performed on the two samples. For the 30% Mn-doped sample (Fig. 2a and b), the experimental atomic percentages vary significantly with the analyzed area. For instance, area A (Fig. 2a) is more Zn^{2+}-rich than expected and the zinc/aluminum ratio is inverted compared with area B (Fig. 2b). Although the global compositions of the whole polycrystalline aggregates are very close to the theoretical composition ($Zn_{0.7}Mn_{0.3}Al_2O_4$), the intra-agglomerate inhomogeneity shows the lack of miscibility of manganese and zinc in this region of the $ZnAl_2O_4$–$MnAl_2O_4$ binary phase diagram through the Pechini process here used. Moreover, at this Mn doping rate, the limit of manganese and zinc miscibility is reached, resulting in compositional heterogeneity and the formation of a secondary crystalline phase, which is not a manganese oxide as expected, but an α-Al_2O_3 aluminate. Hence, the lack of miscibility for the high manganese doping rate seems to be a consequence of competition between the substitution of Mn^{2+} for Zn^{2+} and the substitution of Mn^{3+} for Al^{3+} ($ZnMn_2O_4$ is also isotropic with $ZnAl_2O_4$).

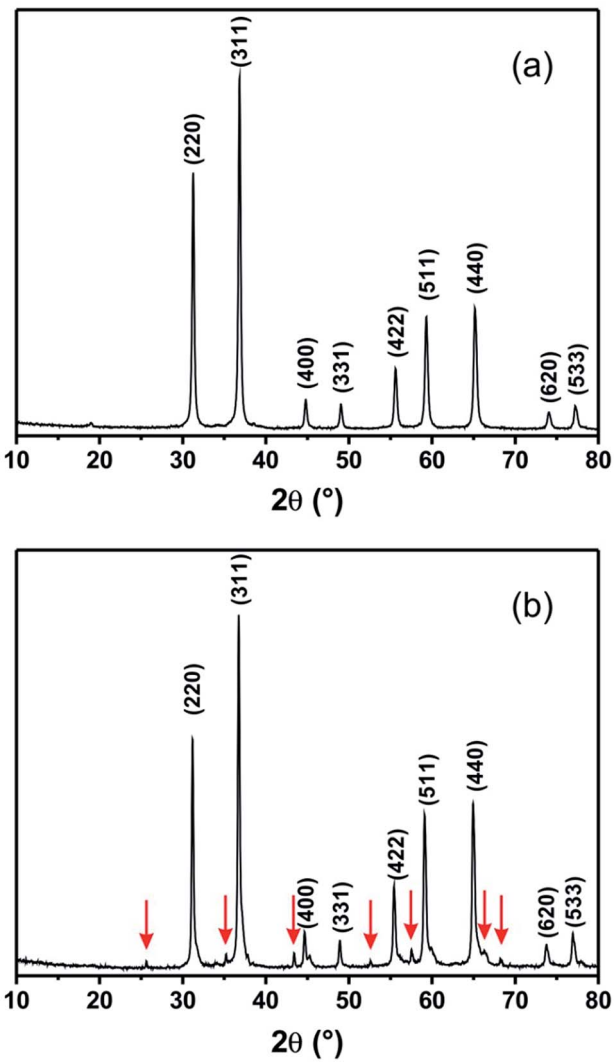

Fig. 1 X-ray diffraction patterns of the samples treated at 1000 °C with compositions of (a) $Zn_{0.85}Mn_{0.15}Al_2O_4$ and (b) $Zn_{0.7}Mn_{0.3}Al_2O_4$. Red arrows show the secondary phase, α-Al_2O_3 corundum.

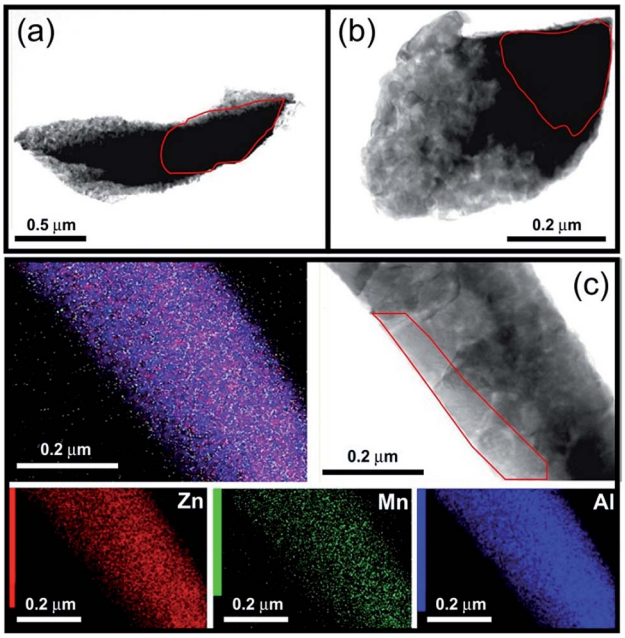

Atomic %	Zn	Mn	Al
zone A	56	14	30
zone B	34	14	52
zone C	30	5	65

Fig. 2 (a) and (b) TEM images of aggregates of the samples treated at 1000 °C with a global composition of $Zn_{0.7}Mn_{0.3}Al_2O_4$, (c) TEM images and EDX-cartographies of the sample treated at 1000 °C with a composition of $Zn_{0.85}Mn_{0.15}Al_2O_4$. Zn, Al and Mn molar percentages calculated from EDX data from areas A, B and C are given in the bottom table.

However, TEM-EDX analyses of the 15% Mn-doped sample (Fig. 2c) show that all the analyzed areas exhibit experimental Zn : Mn : Al ratios close to the theoretical ones, in good agreement with the XRD results, revealing the crystallization of a single spinel phase. The manganese substitution of zinc in $ZnAl_2O_4$ is thus limited to a value between 15% and 30%.

This first study showed that formation of Mn(III) in addition to Mn(II) must be considered in our samples, and consequently, a limit of manganese solubility of about 15%.

Considering the optical behavior of Mn^{2+} and the low threshold of concentration quenching in this matrix, we explored the luminescent properties of a 0.5% doped compound, *i.e.* a value substantially below the manganese solubility limit. Thus, all the properties discussed should only be attributed to the spinel phase.

3.2. Global divalent cation inversion rate ($\delta_{Zn} + \delta_{Mn}'$) from XRD pattern refinements

Rietveld refinements were performed on 0.5% Mn-doped $ZnAl_2O_4$ samples obtained after thermal treatments at temperatures ranging from 500 to 1350 °C. Experimental and calculated spectra of the samples annealed at 600 and 1200 °C are presented in Fig. 3.

The X-ray spectra in Fig. 3 show that a pure spinel form is obtained whatever the synthesis temperature. Considering the composition formulae $(Zn_{0.995-\delta}Mn_{0.005-\delta'}Al_{\delta+\delta'})$-$[Zn_{\delta}Mn_{\delta'}Al_{2-\delta-\delta'}]O_4$, only the global inversion rate ($\delta + \delta'$) of A^{2+} divalent cations can be determined from X-ray refinements. Indeed, the low doping level in Mn^{2+} ions and the proximity of the atomic number of Mn and Zn do not allow us to estimate the manganese occupancies accurately. Therefore, the structural refinements were performed considering the chemical formula $(Zn_{1-\delta-\delta'}Al_{\delta+\delta'})[Zn_{\delta+\delta'}Al_{2-\delta-\delta'}]O_4$. The evolution of the cell parameter, crystallite size and inversion rate with the annealing temperature are presented in Table 1 and Fig. 4. The annealing temperature has a notable effect on the crystallite size and on the global inversion rate, whereas no significant variation of the cell parameter was observed. As the temperature increased, the sintering effect induced crystallite growth from about 20 nm at 500 °C to 120 nm at 1350 °C, and the global inversion rate decreased gradually from 16% to 2.6% (Fig. 4). The effect of crystallite size on the cationic distribution appears secondary; the crystallite size almost doubled between 1000 and 1200 °C whereas the inversion rate remained stable. In contrast, the

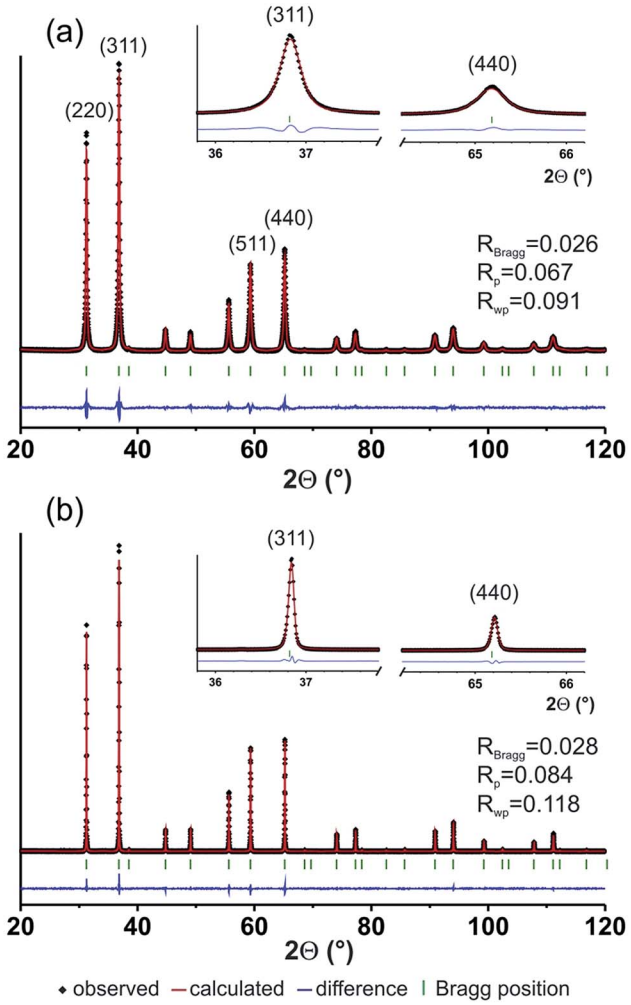

Fig. 3 Refined X-ray diffractograms (experimental, calculated and difference) for 0.5% Mn-doped $ZnAl_2O_4$ samples obtained after thermal treatment at (a) 600 and (b) 1200 °C.

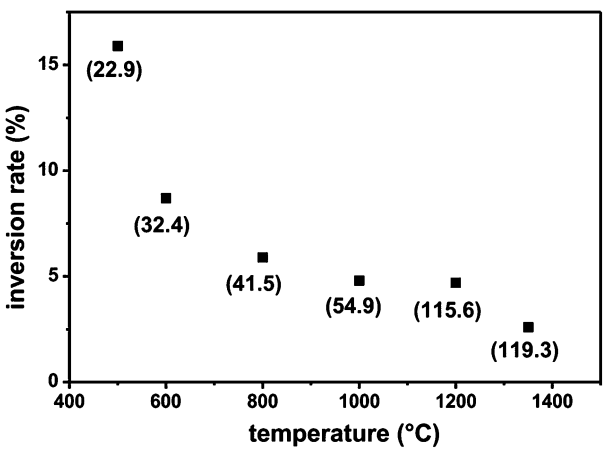

Fig. 4 Global A^{2+} divalent cations inversion rate *versus* the temperature of the post-thermal treatment for the 0.5% Mn-doped $ZnAl_2O_4$ sample. The 0.5% Mn-doped $ZnAl_2O_4$ crystallite sizes (in nm) are reported in parentheses.

Table 1 Structural parameters of the 0.5% Mn-doped $ZnAl_2O_4$ samples obtained after various thermal treatments

				Reliability factors[b]		
Synthesis T (°C)	Crystallite size (nm)	Cell parameter (Å)	Inversion rate[a] (%)	R_p	χ^2	R-Bragg
500	22.9	8.09 (5)	15.9	0.051	4.0	0.042
600	32.4	8.08 (9)	8.7	0.067	5.0	0.026
800	41.5	8.09 (5)	5.9	0.058	4.0	0.028
1000	54.9	8.084 (5)	4.8	0.061	3.8	0.023
1200	115.6	8.089 (4)	4.7	0.084	2.5	0.028
1350	119.3	8.087 (4)	2.6	0.121	2.2	0.039

[a] Global inversion rate ($\delta + \delta'$). [b] With all-non excluded models and not corrected for background.

annealing temperature appears to play a key role in the cationic distribution within the spinel structure and may influence the optical properties of the treated samples.

3.3. Optical properties

The optical properties of Mn-doped $ZnAl_2O_4$ depend on the location of Mn^{2+} ions within the spinel network. When Zn^{2+} is substituted with Mn^{2+} phosphor ions, they can occupy octahedral or tetrahedral sites, depending on synthesis parameters, especially the annealing temperature (as shown above). In previous work,[27] we highlighted the influence of the annealing temperature on the optical properties of undoped $ZnAl_2O_4$ synthesized using the Pechini route. A drastic change in the diffuse reflectance spectra was observed as the temperature increased from 1200 to 1350 °C. This last thermal treatment led to the total migration of zinc cations into the tetrahedral coordination polyhedra, and a blue shift of the front absorption from 400 to 300 nm was observed. Fig. 5 shows diffuse reflectance spectra of manganese-doped $ZnAl_2O_4$ as a function of the doping level for samples annealed at 1200 and 1350 °C.

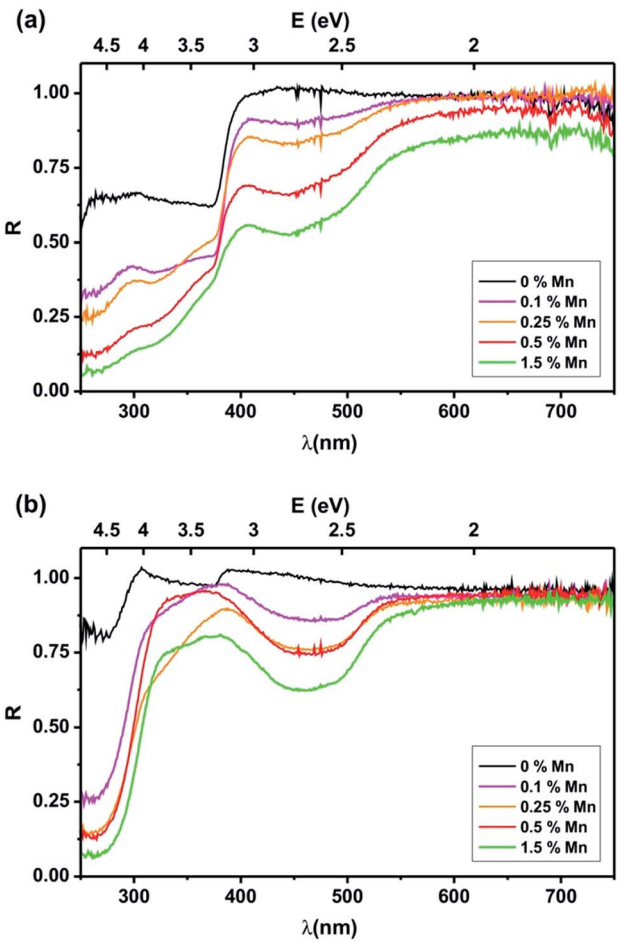

Fig. 5 Diffuse reflectance spectra of various Mn-doped $ZnAl_2O_4$ samples for different Mn^{2+} concentrations obtained after thermal treatment at 1200 (a) and at 1350 °C (b).

As observed for the undoped matrix, the contribution of the Zn–O charge transfer band for the six fold-coordinated zinc ions located at 400 nm disappears after heat treatment at 1350 °C. The Zn–O charge transfer that occurs in the tetrahedral zinc environment is then visible at 300 nm. The larger the amount of manganese, the larger the absorption centered at 460 nm. Considering the low probability of the 3d–3d forbidden transition for divalent manganese, this band is probably due to intervalence absorption or to manganese ions in a higher oxidation state. The depletion of aluminum from the spinel phase discussed earlier could be responsible for the occurrence of trivalent or tetravalent Mn^{n+} ($R_{Mn^{3+}} = 0.66$ Å; $R_{Mn^{4+}} = 0.54$ Å), which may easily replace Al^{3+} ($R_{Al^{3+}} = 0.53$ Å) in an octahedral environment.

The luminescence spectra of various Mn-doped compositions recorded at 300 K for the optimal excitation wavelength at 426 nm are presented in Fig. 6. Despite the occurrence of defects in the spinel compounds obtained at this thermal treatment temperature and non-negligible associated photoluminescence (PL), as shown in our previous work,[27] the $ZnAl_2O_4$ matrix appears non-luminescent for an excitation at 426 nm when directly compared with Mn-doped compounds. It can be clearly seen that all the compositions exhibit roughly the same spectral distribution (same Gaussian shape centered on the same wavelength), with only the intensities diverging. The 0.5% Mn-doped compound produces a higher photoluminescence response. The dependence of the PL intensity on the doping element concentration is usually described for luminescent materials; it shows a concentration quenching threshold at a molar substitution of about 0.5%. Thus, we decided to focus the characterization studies on the optimized compound to ensure an accurate description.

The next part of the study focused on the 0.5% doped material. The evolution of the absorption with the annealing temperature is presented in Fig. 7. A drastic change in the diffuse reflectance spectra was observed for $T > 1200$ °C, thus only the samples treated at 1200 and 1350 °C are discussed. Fig. 8 shows the excitation and emission spectra recorded for

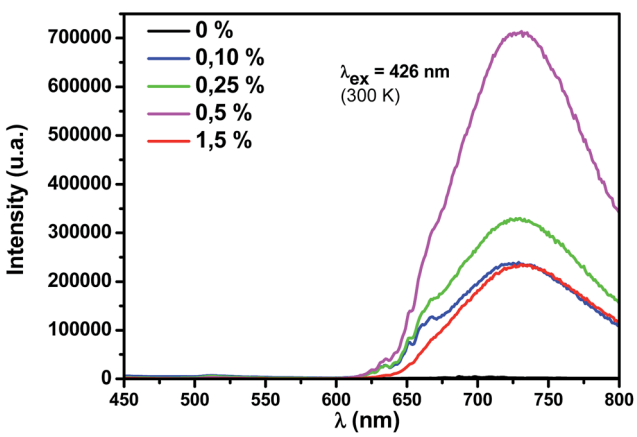

Fig. 6 Luminescence spectra of various Mn-doped $ZnAl_2O_4$ heat treated at 800 °C under air and annealed under argon–hydrogen at 500 °C.

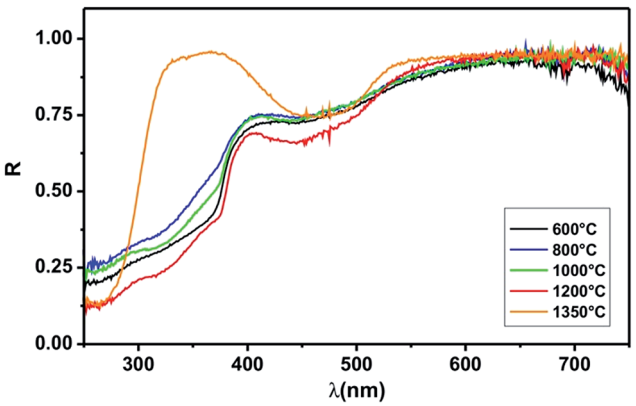

Fig. 7 Diffuse reflectance spectra of 0.5% Mn-doped $ZnAl_2O_4$ samples obtained after various thermal treatments.

the samples obtained after annealing at these two temperatures.

At 1350 °C, the total direct Mn-doped spinel produced the expected green luminescence (Fig. 8c) that is reported in many papers for divalent manganese in a tetrahedral environment.[28–31] Considering the site preference energies of Mn^{2+} and Al^{3+} (−14.7 kcal m^{-1} and −2.5 kcal m^{-1} respectively), divalent manganese ions may preferentially adopt tetrahedral coordination.[32] The main $^4T_1 \rightarrow {}^6A_1$ transition peaks at 508 nm and the sideband vibronic vibrations are detected at lower energies, with peaks at 514, 520 and 529 nm, respectively. Table 2 lists the splitting of the different energy level observed at 10 K (Fig. 8c). The $^6A_1 \rightarrow {}^4T_1$ (^4G) absorption component is not observed because the Stokes shift is too small and the experimental acquisition conditions are not appropriate. The $^6A_1 \rightarrow {}^4T_{2g}$ (^4G) triplet absorption line is well resolved whereas a unique line is detected for the $^6A_1 \rightarrow {}^4E_g/{}^4A_{1g}$ (^4G) transitions. Finally, two doublets can be attributed to the $^6A_1 \rightarrow {}^4T_{2g}$ (^4D) and $^6A_1 \rightarrow {}^4E_g$

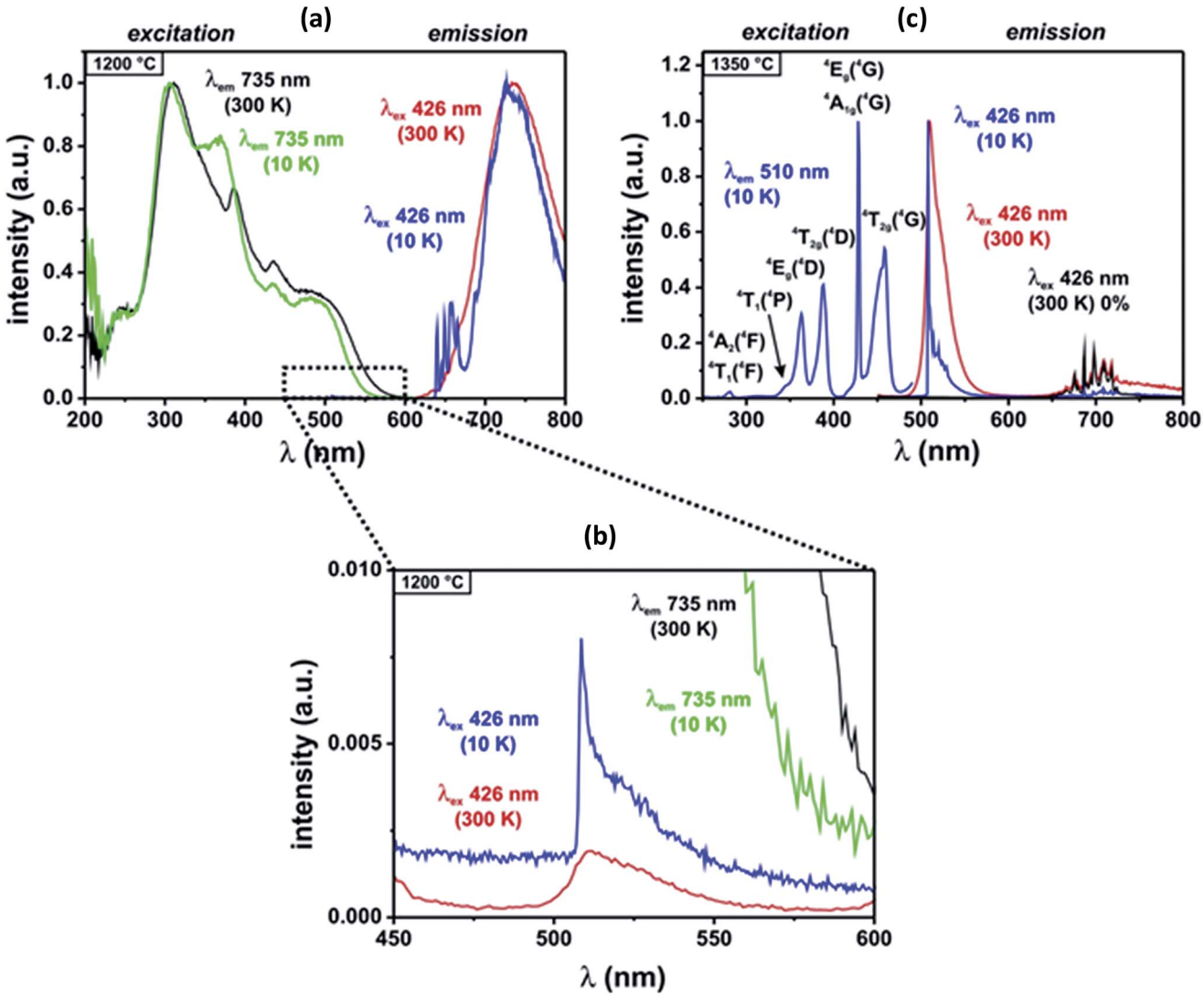

Fig. 8 Luminescence spectra of the 0.5% Mn-doped $ZnAl_2O_4$ sample after thermal treatment at (a) 1200 °C, (b) magnification of the 450–600 nm range in (a), and at (c) 1350 °C.

Table 2 Splitting of Mn^{2+} energy levels in $ZnAl_2O_4$

Energy level of free Mn^{2+} ion ($3d^5$)	Energy level in T_d or O_h sites	Observed transitions/excitation in nm (cm^{-1})	
		Compound annealed at 1350 °C (4-fold coordinated Mn^{2+})	Compound annealed at 1200 °C (5/6-fold coordinated Mn^{2+})
^4G	$^4T_{1g}$	Not observed	Not observed
	$^4T_{2g}$	434 (23 041) < λ_{ex} < 475 (21 052)	462 (21 645) < λ_{ex} < 559 (17 889)
	$^4E_g/^4A_{1g}$	428 (23 364)	434 (23 041)
^4D	$^4T_{2g}$	388 (25 773)	369 (27 100)
	^4E_g	363 (27 548)	352 (28 409)

(^4D) transitions. The decay time value of this green emission is equal to 4.8 ms (measurement performed for an excitation at 426 nm and an emission at 510 nm), which is close to the values reported in literature.[33] The value was calculated using a bi-exponential fitting model. A secondary faster component (0.3 ms) is also observed indicating competitive de-excitation that might be caused by matrix defects.

For an excitation at 426 nm, red emission lines were also detected between 640 and 730 nm. Considering the diffuse reflectance spectra of the doped (Fig. 7) and undoped $ZnAl_2O_4$ matrix,[27] these emission lines are due to traces of Cr^{3+} luminescing, as observed in the undoped materials. Isoelectronic Mn^{4+} could also contribute to this emission; the presence of Mn^{4+} will be discussed later. However, because of the high similarity of the two spectral distributions, their respective contribution to the whole spectrum cannot be separated, at least under these experimental conditions.

The luminescence properties of the sample annealed at 1200 °C revealed that a significant amount of manganese ions are not four-fold coordinated (Fig. 8a). The emission spectrum obtained under an excitation of 426 nm clearly shows a large band centered at 738 nm. The emission spectrum of the undoped matrix confirms that this red luminescence is related to the introduction of manganese to the partially indirect spinel network. As demonstrated in a previous study,[27] the optical properties of the spinel heat treated at 1200 °C are directly linked to the occurrence of punctual defects. The red luminescence obtained for excitation at 370 nm has been related to the presence of oxygen vacancies around the Zn_{Al} anti-site. This emission is not observed with an excitation at 426 nm. Therefore, some manganese ions with a valence higher than two could be localized either in these distorted five-fold coordinated polyhedra or in regular AlO_6 octahedra, substituting for Al^{3+}. Mn^{4+} luminescence has already been mentioned in the previous paragraph. Moreover, no additional spectral distribution caused by Mn^{3+} was observed. Nevertheless, even if Mn^{3+} was stabilized in this matrix, the associated luminescence could not be observed because of a strong Jahn–Teller effect.[29] Based on this information, we assumed that the reducing heat-treatment applied during the chosen synthetic route successfully stabilized the divalent manganese ions in anti-site (divalent cation in the Al^{3+} site) with a coordination number higher than 4, leading to the red emission observed for the Mn-doped $ZnAl_2O_4$ spinels. Moreover, the shape of the excitation spectrum (large component) indicates that the crystallographic environment of the doping ions is not well-defined and regular. Decay time measurements were performed for excitation and emission wavelengths of 426 and 735 nm respectively. The experimental decay curve was decomposed into two equally weighted components with different decay time values of 50 and 250 μs, which are close to those reported for the red emission of Mn^{2+}.[34]

The optical transition rules were modified when the symmetry around the element was changed (more strictly parity forbidden). This observation does not exclude the fact that part of the divalent manganese should be localized in the tetrahedra. A magnified view of the 450–650 nm range (Fig. 8b) clearly shows a weak green emission; however, the spectral distribution of the red luminescence excitation spectrum indicates that if it occurs, this green emission is mainly reabsorbed.

3.4. Al-overstoichiometric phases, $Zn_{0.995}Mn_{0.005}Al_{2.2}O_{4+\delta}$

In order to understand the coupling between the octahedral occupancy of manganese and the temperature better, a compound containing an excess of aluminum atoms was prepared. A 0.5% Mn-doped $ZnAl_{2.2}O_4$ sample was heat-treated at 800, 1000 and 1200 °C. The overstoichiometry of oxygen was retained to simplify the description; the anionic sub-network in spinel that forms a slightly distorted rocksalt-like anionic framework means that supplementary anions could not be inserted into the structure. Compensation for the Al-overstoichiometry was achieved from cationic vacancies in both tetrahedral and octahedral sites. The crystallite sizes calculated by Rietveld refinement were 27, 40 and 58 nm for the samples from the lowest to the highest annealing temperature, respectively. The corresponding inversion rates of 2.92%, 1.20% and 0% for the lowest to the highest annealing temperature, respectively, were smaller than those calculated for the stoichiometric sample. This indicates that it is more difficult to introduce a divalent cation in the octahedral position.

Regarding the new luminescent properties (Fig. 9), divalent manganese cations migration from the octahedral to the tetrahedral location is detected from 800 °C and is complete at 1200 °C. The relative maximum intensity between the two luminescences varies from 0.042 (I_{max510}/I_{max733} 800 °C), 1.41 (1000 °C) to 40.43 (1200 °C) for the Al^{3+}-overstoichiometric sample in comparison with a value equal to 0.006 for the 1200 °C-annealed stoichiometric sample (Fig. 9). For Mn-doped

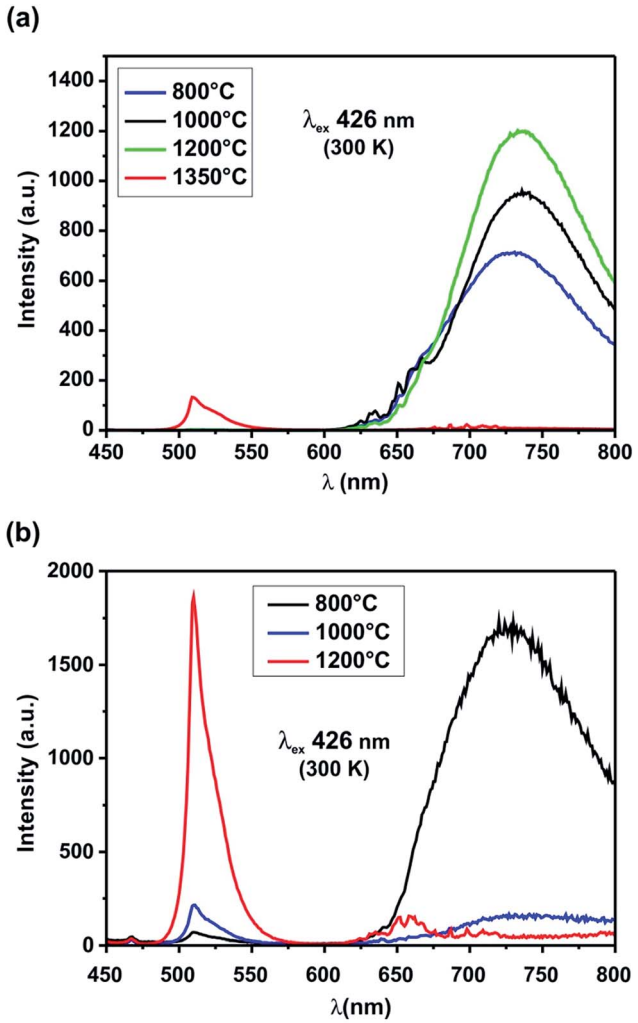

Fig. 9 Luminescence spectra of 0.5% Mn-doped (a) $ZnAl_2O_4$ and (b) $ZnAl_{2.2}O_{4+\delta}$ samples annealed at various temperatures.

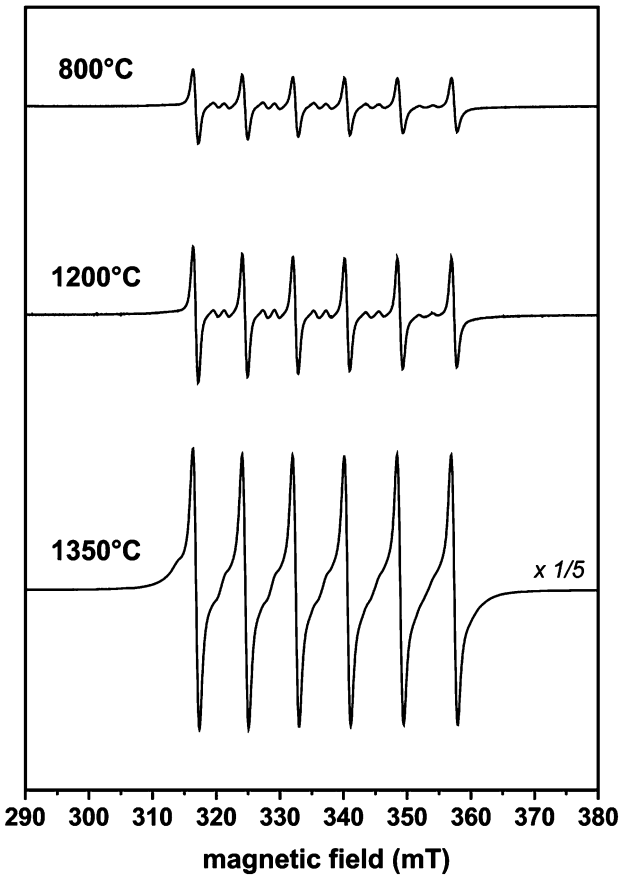

Fig. 10 Room temperature X-band EPR spectra of 0.5% Mn-doped $ZnAl_2O_4$ annealed at 800, 1200 and 1350 °C.

$ZnAl_{2.2}O_4$ materials, a larger temperature range is accessible to modulate the expected visible emission. The evolution of luminescence properties with the thermal treatment temperature is directly related to the stabilization of the manganese cations in tetrahedral sites. Hence, from varying the matrix chemical composition, the preferential octahedral or tetrahedral site occupancy of the constituting cations can be understood and altered, and the red to green emission switch can be tuned at lower temperatures opening a wide range of applications for these material series as thermal sensors.

3.5. Electron paramagnetic resonance study

Polycrystalline samples of 0.5% mol Mn-doped $ZnAl_2O_4$ and $ZnAl_{2.2}O_{4+\delta}$ annealed at temperatures ranging from 800 to 1350 °C were analyzed by EPR spectroscopy.

The spectra presented in Fig. 10 and 11 are characteristic of Mn^{2+} ions ($3d^5$: ^6S ground state, $S = 5/2$, $I = 5/2$) and can be described by the spin Hamiltonian:

$$H = g\beta H\cdot S + S\cdot D\cdot S + AS\cdot I \quad (1)$$

The first term of eqn (1) represents the Zeeman interaction, where g is the g factor, β the Bohr magneton and H the applied magnetic field. The second term is the zero-field splitting term which can be written

$$D\left[S_z^2 - \frac{1}{3}S(S+1)\right] + E\left(S_x^2 - S_y^2\right) \quad (2)$$

where D and E are the zero-field splitting parameters ($-1 \leq 3E/D \leq 0$ in the standard range). The third term arises from the hyperfine interaction with the Mn nuclear spin (I) where A is the hyperfine coupling constant whose value is directly linked to the ionicity of the metal–ligand bonds, at least when Mn^{2+} is in a cubic or nearly cubic crystal field.[35] In this work, the g factor and the hyperfine coupling constant can be reasonably considered isotropic and, according to previous studies,[36] the cubic zero-field splitting term that could be added to the spin Hamiltonian (1) is neglected.

The Mn^{2+} EPR signal consists of six ($2I$ + 1) main lines (Fig. 10 and 11) corresponding to the allowed transitions ($\Delta m = 1$) between the $|+1/2, m\rangle$ and $|-1/2, m\rangle$ levels, where m is the nuclear spin magnetic quantum number, $-5/2 \leq m \leq +5/2$. The other four allowed transitions ($\Delta M = \pm 1$, $\Delta m = 0$; M, electronic spin magnetic quantum number, $-5/2 < M \leq +5/2$) are strongly dependent on the zero-field splitting terms D and E in the first

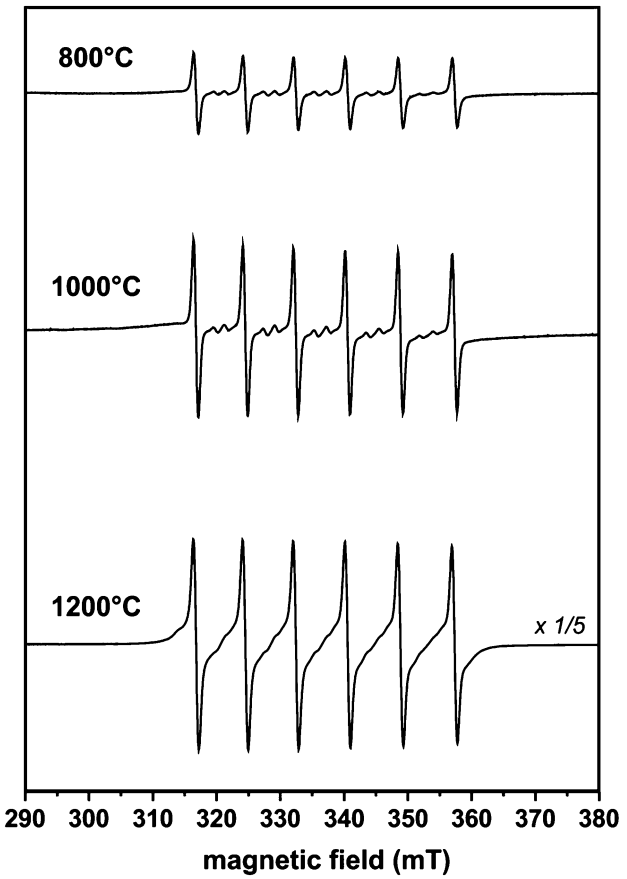

Fig. 11 Room temperature X-band EPR spectra of 0.5% Mn-doped $ZnAl_{2.2}O_{4+\delta}$ annealed at 800, 1000 and 1200 °C.

order and are generally not resolved in powder spectra. In between each of the six allowed lines, the five doublets are associated with forbidden transitions ($\Delta m = \pm 1$) arising from the second order perturbation of the nuclear hyperfine levels by the zero-field splitting.[37] According to Shaffer *et al.*,[38] the ratio of the intensities of the forbidden lines, I_f, to the allowed lines, I_A, is given by eqn (3), obtained by neglecting the E term of the spin Hamiltonian (eqn (1)).

$$\frac{I_f}{I_A} = \frac{512}{15}\left(\frac{35}{4} - m^2 + m\right)\left(\frac{D^*}{g\beta H}\right)^2 \quad (3)$$

This parameter can also be roughly estimated from polycrystalline EPR spectra by measuring the relative intensities of the allowed lines.[39,40] Nevertheless, an accurate evaluation of the D and E values generally requires EPR analysis of single crystals.

The values of $g = 2.0015 \pm 0.0002$ and $|A| = 76 \pm 1 \times 10^{-4}$ cm^{-1} calculated for the observed signals (Table 3) are close to those already reported for Mn^{2+} ions in ZnO (ref. 41) in $MgAl_2O_4$ (ref. 38 and 42) and $ZnAl_2O_4$ (ref. 25 and 36) spinels where Mn^{2+} is assumed to be substituted for the divalent cation at tetrahedral A sites of the spinel structure. It is worth noting that the assignment to octahedral or tetrahedral sites is difficult without complementary information, such as structural features or optical properties.

However, none of the samples exhibits a Mn^{4+} ($3d^3$: $^4A_2$ ground state, $S = 3/2$, $I = 5/2$) signal with a g-value (1.994 ± 0.001);[43,44] which is significantly different from the Mn^{2+} signal ($g > 2.000$).[45] Therefore, the increase in EPR signal intensity with annealing temperature (Fig. 10) may arise from the reduction of Mn^{3+} ($3d^4$, EPR silent) to Mn^{2+}, which appears to be fully achieved after thermal treatment at 1350 °C. The number of spins responsible for the EPR signal of the Mn:$ZnAl_2O_4$ sample annealed at 1350 °C corresponds to 0.49 (8) mol% of Mn^{2+} ions, which is close to the initial Mn doping level (Table 3). Moreover, for Mn-doped $ZnAl_{2.2}O_{4+\delta}$, only half of the manganese ions are in the (II) oxidation state after thermal treatment at 1200 °C (Table 3), revealing the effect of the annealing temperature on the Mn^{2+}/Mn^{3+} ratio within the spinel matrix. A similar evolution of the Mn^{2+} EPR signal with temperature was reported by Su Kim *et al.*[46] for Mn-doped $ZnGa_2O_4$ phosphors annealed at temperatures ranging from 700 to 1100 °C.

The oxidation states and the ionic radii of the doping ions (Mn^{2+}: 0.80 Å; Mn^{3+}: 0.66 Å) and substituted cations (Zn^{2+}: 0.74 Å; Al^{3+}: 0.53 Å) indicate that Mn^{3+} ions should preferentially occupy the octahedral B sites and Mn^{2+} should occupy the tetrahedral A sites. However, we previously showed that the cationic distribution within the $ZnAl_2O_4$ matrix and the occurrence of punctual defects (*e.g.* oxygen vacancies) are clearly

Table 3 EPR parameters for Mn^{2+} signal in 0.5% Mn-doped $ZnAl_2O_4$ and 0.5% Mn-doped $ZnAl_{2.2}O_{4+\delta}$ obtained after various thermal treatments. g factor; hyperfine coupling constant, $|A|$; zero-field splitting parameter, D^*; peak-to-peak line width, ΔH_{pp}; and number of spins, N (associated with the observed signal)

Synthesis T°	g factor	$\lvert A\rvert$ ($\times 10^{-4}$ cm^{-1})	D^* ($\times 10^{-4}$ cm^{-1})	ΔH_{pp} (mT)	N ($\times 10^{20}$)	$[Mn^{2+}]$ (%mol.)
0.5% Mn-doped $ZnAl_2O_4$						
800 °C	2.0016(2)	76(1)	58(2)	0.6(1)	0.026(1)	0.016(1)
1200 °C	2.0015(2)	76(1)	49(2)	0.6(1)	0.048(2)	0.029(1)
1350 °C	2.0014(2)	76(1)	26(1)	1.0(1)	0.804(8)	0.490(8)
0.5% Mn-doped $ZnAl_{2.2}O_{4+\delta}$						
800 °C	2.0016(2)	76(1)	45(2)	0.7(1)	0.022(1)	0.013(1)
1000 °C	2.0015(2)	76(1)	34(1)	0.7(1)	0.038(1)	0.023(1)
1200 °C	2.0013(2)	76(1)	10(1)	0.8(1)	0.382(9)	0.235(8)

influenced by the annealing temperature (Fig. 4). Thus, Mn-doped $ZnAl_2O_4$ samples annealed at $T \leq 1200$ °C may contain Mn^{2+} ions in anti-sites (B sites) with a coordination number higher than 4. The resulting distortion of the manganese environment may then induce a significant change in the Mn^{2+} EPR signal, *i.e.* increase the forbidden line intensity and modify the relative intensities of the allowed hyperfine lines.

This data indicates that the EPR spectra presented in Fig. 10 and 11 are the sum of two signals associated with 4-fold and 5/6-fold coordinated Mn^{2+} ions, respectively. As the annealing temperature increases, the global divalent cation inversion rate and the number of defects (oxygen vacancies) decrease, thus, the relative proportion of these two EPR signals may change. Indeed, the signal of Mn^{2+} becomes more regular, reflected in the decrease in the D^* parameter (Table 3), revealing a less distorted environment for Mn^{2+} ions. Then, the EPR spectra of the samples annealed at high temperature (1350 °C for Al-stoichiometric samples and 1200 °C for Al-overstoichiometric samples) may be associated with Mn^{2+} ions in tetrahedral sites (Zn^{2+} site) in a direct spinel structure. This is in good agreement with the optical properties that show a drastic increase in the T_d-Mn^{2+} emission for Mn-doped $ZnAl_2O_4$ spinels annealed at 1350 °C and for Mn-doped $ZnAl_{2.2}O_{4+\delta}$ phosphors synthesized at 1200 °C (see previous section).

4. Conclusions

This study shows that the thermal history of $ZnAl_2O_4$ spinels doped with manganese ions has a strong influence on their optical properties. The structural features of the as-prepared samples indicate that the solubility limit is reached for a high manganese concentration (between 15 and 30 mol%). Moreover, the cationic distribution for 0.5 mol%-doped $ZnAl_2O_4$ samples obtained after various thermal treatments was monitored by XRD and EPR analyses. From the XRD data, the structural refinements show that the global inversion rate (Zn + Mn) decreases with the annealing temperature. The EPR results revealed a clear change in the local environment of Mn^{2+} within the spinel matrix and an increase in the amount of Mn^{2+}, due to the reduction of Mn^{3+} ions. The divalent manganese cations progressively and irreversibly migrate from the octahedral to the tetrahedral sites. The variations of luminescence properties are directly related to the change in inversion rate. The samples treated at low temperatures exhibit a red luminescence, characteristic of manganese in octahedral sites. As the annealing temperature increases, the inversion rate decreases and a green emission associated with divalent manganese ions in a tetrahedral environment is observed. Furthermore, a low amount of manganese in octahedral sites is required to prevent re-absorption that could reduce or quench the green luminescent emission. Finally, the temperature range and the kinetics of this luminescence switch can be modified by modulating the spinel matrix composition. The irreversible change in the luminescence properties of this material according to its thermal history means it may be suitable as a thermal sensor.

Acknowledgements

Lucile Cornu is the holder of the doctoral fellowship supported by the Bordeaux 1 University. The authors thank CNRS, the Aquitaine region, the LaPhIA and the ANR (ANR-2010-BLANC-0820) for financial support. The authors also thank J. Majimel for TEM-EDX investigations.

Notes and references

1 J. Wrzyszcz, M. Zawadzki, J. Trawczynski, H. Grabowska and W. Mista, *Appl. Catal., A*, 2001, **210**(1–2), 263.
2 F. Le Peltier, P. Chaumette, J. Saussey, M. M. Bettahar and J. C. Lavalley, *J. Mol. Catal. A: Chem.*, 1997, **122**(2–3), 131.
3 T. K. Parya, R. K. Bhattacharyya, S. Banerjee and U. B. Adhikari, *Ceram. Int.*, 2010, **36**(4), 1211.
4 C. Angeletti, F. Pepe and P. Porta, *J. Chem. Soc., Faraday Trans. 1*, 1977, **73**, 1972.
5 J.-M. Lu, W.-Z. Lu, W. Lei and X.-C. Wang, *Mater. Res. Bull.*, 2011, **46**(9), 1485.
6 S. K. Sampath and J. F. Cordaro, *J. Am. Ceram. Soc.*, 1998, **81**(3), 649.
7 A. Fernandez-Osorio, E. Pineda-Villanueva and J. Chavez-Fernandez, *Mater. Res. Bull.*, 2012, **47**(2), 445.
8 M. Gaudon, A. Apheceixborde, M. Menetrier, A. Le Nestour and A. Demourgues, *Inorg. Chem.*, 2009, **48**(19), 9085.
9 A. Le Nestour, M. Gaudon, G. Villeneuve, M. Daturi, R. Andriessen and A. Demourgues, *Inorg. Chem.*, 2007, **46**(10), 4067.
10 M.-T. Tsai, Y.-F. Lu and Y.-K. Wang, *J. Alloys Compd.*, 2010, **505**(2), 818.
11 J. Popovic, B. Grzeta, B. Rakvin, E. Tkalcec, M. Vrankic and S. Kurajica, *J. Alloys Compd.*, 2011, **509**(34), 8487.
12 M.-T. Tsai, Y.-S. Chang, I.-B. Huang and B.-Y. Pan, *Ceram. Int.*, 2013, **39**(4), 3691.
13 I. Mindru, G. Marinescu, D. Gingasu, L. Patron, L. Diamandescu, C. Ghica and B. Mironov, *Mater. Sci. Eng., B*, 2010, **170**(1–3), 99.
14 B. S. Barros, P. S. Melo, R. H. G. A. Kiminami, A. C. F. M. Costa, G. F. de Sa and S. Alves Jr, *J. Mater. Sci.*, 2006, **41**(15), 4744.
15 Z. Lou and J. Hao, *Thin Solid Films*, 2004, **450**(2), 334.
16 K. H. Winbow and J. Cowley, *Ceram. Eng. Sci. Proc.*, 1996, **17**(1), 102.
17 R. F. Cooley and J. S. Reed, *J. Am. Ceram. Soc.*, 1972, **55**, 395.
18 J. Popovic, E. Tkalcec, B. Grzeta, S. Kurajica and B. Rakvin, *Am. Mineral.*, 2009, **94**, 771.
19 J. C. Waerenborgh, M. O. Figueiredo, J. M. P. Cabral and L. C. J. Pereira, *J. Solid State Chem.*, 1994, **111**(2), 300.
20 A. LeNestour, Corrélation structure-propriétés d'absorption UV-Vis-IR associée aux états de valence du cuivre dans des oxydes à base de zinc de type spinelle et würtzite, PhD thesis, Université Bordeaux 1, April 2006.
21 H. Matsui, C.-N. Xu, Y. Liu and H. Tateyama, *Phys. Rev. B: Condens. Matter Mater. Phys.*, 2004, **69**, 235109.
22 N. J. van der Laag, M. D. Snel, P. C. M. M. Magusin and G. de With, *J. Eur. Ceram. Soc.*, 2004, **24**(8), 2417.

23 M. Vasile, P. Vlazan and N. M. Avram, *J. Alloys Compd.*, 2010, **500**(2), 185.
24 L. Torkian, M. M. Amini and Z. Bahrami, *J. Inorg. Mater.*, 2011, **26**(5), 550.
25 V. Singh, R. P. S. Chakradhar, J. L. Rao and D.-K. Kim, *J. Lumin.*, 2008, **128**, 394.
26 M. P. Pechini, *U.S. Pat.* no. 3231328, January 1966.
27 L. Cornu, M. Gaudon and V. Jubera, *J. Mater. Chem. C*, 2013, **1**, 5419.
28 T. Koskentalo, M. Leskelä and L. Niinistö, *Mater. Res. Bull.*, 1985, **20**(3), 265.
29 A. van Die, A. C. H. I. Leenaers, W. F. van der Weg and G. Blasse, *Mater. Res. Bull.*, 1987, **22**, 781.
30 R. Mlcak and A. H. Kitai, *J. Lumin.*, 1990, **46**(6), 391.
31 G. Li, D. Geng, M. Shang, C. Peng, Z. Cheng and J. Lin, *J. Mater. Chem.*, 2011, **21**, 13334.
32 S. Geschwind, P. Kisliuk, M. P. Klein, J. P. Remeika and D. L. Wood, *Phys. Rev.*, 1962, **126**, 1684.
33 S. Shionoya, W. M. Yen and H. Yamamoto, *Phosphor Handbook*, 2nd edn, 2007.
34 U.-C. Chung, J. L. Mesa, J. L. Pizarro, V. Jubera, L. Lezama, M. I. Arriortua and T. Rojo, *J. Solid State Chem.*, 2005, **178**, 2913.
35 O. Matumura, *J. Phys. Soc. Jpn.*, 1959, **14**(1), 108.
36 R. Stahl-Brada and W. Low, *Phys. Rev.*, 1959, **116**(3), 561.
37 E. Friedman and W. Low, *Phys. Rev.*, 1960, **120**(2), 408.
38 J. S. Shaffer, H. A. Farach and C. P. Poole Jr, *Phys. Rev. B: Solid State*, 1976, **13**(5), 1869.
39 C. P. Poole Jr, H. A. Farach and W. K. Jackson, *J. Chem. Phys.*, 1974, **61**(6), 2220.
40 B. T. Allen, *J. Chem. Phys.*, 1965, **43**(11), 3820.
41 P. B. Dorain, *Phys. Rev.*, 1958, **112**(4), 1058.
42 V. Singh, R. P. S. Chakradhar, J. L. Rao and K. Dong-Kuk, *J. Solid State Chem.*, 2007, **180**, 2067.
43 S. Geschwind, P. Kisliuk, M. P. Klein, J. P. Remeika and D. L. Wood, *Phys. Rev.*, 1962, **126**(5), 1684.
44 S. Tanaka, K. Mizushima and S. Ida, *J. Phys. Soc. Jpn.*, 1978, **45**(1), 133.
45 A. Abragam and B. Bleaney, *Electron Paramagnetic Resonance of Transition ions*, Clarendon Press, 1970.
46 J. Su Kim, J. Su Kim, T. Wan Kim, S. Myung Kim and H. Lee Park, *Appl. Phys. Lett.*, 2005, **86**, 091912.